

# Spin reorientation, magnetization reversal, and negative thermal expansion observed in $R\text{Fe}_{0.5}\text{Cr}_{0.5}\text{O}_3$ perovskites ( $R = \text{Lu}, \text{Yb}, \text{Tm}$ )

Fernando Pomiro,<sup>1</sup> Rodolfo D. Sánchez,<sup>2</sup> Gabriel Cuello,<sup>3</sup> Antoine Maignan,<sup>4</sup> Christine Martin,<sup>4</sup> and Raúl E. Carbonio<sup>1,\*</sup>

<sup>1</sup>INFIQC (Consejo Nacional de Investigaciones Científicas y Técnicas [CONICET]–Universidad Nacional de Córdoba), Departamento de Físicoquímica, Facultad de Ciencias Químicas, Universidad Nacional de Córdoba, Haya de la Torre Esq. Medina Allende, Ciudad Universitaria, X5000HUA Córdoba, Argentina

<sup>2</sup>Centro Atómico Bariloche, Comisión Nacional de Energía Atómica and Instituto Balseiro, Universidad Nacional de Cuyo, (8400) San Carlos de Bariloche (RN), Argentina

<sup>3</sup>Institut Laue-Langevin (ILL), BP 156, F-38042 Grenoble Cedex 9, France

<sup>4</sup>Laboratoire CRISMAT, UMR 6508 Centre national de la recherche scientifique (CNRS)/ENSICAEN/UCBN, 6 Boulevard Marechal Juin, 14050 Caen cedex, France

(Received 6 November 2015; revised manuscript received 12 September 2016; published 3 October 2016)

Three members of the perovskite family  $R\text{Fe}_{0.5}\text{Cr}_{0.5}\text{O}_3$  ( $R = \text{Lu}, \text{Yb}$ , and  $\text{Tm}$ ) have been synthesized and characterized. A systematic study of the crystal and magnetic structures was performed by neutron powder diffraction combined with magnetization measurements. All these compounds crystallize in a  $Pbnm$  orthorhombic unit cell and they are already antiferromagnetic at room temperature. The study of the magnetic structure vs temperature showed the occurrence of a progressive spin reorientation from  $\Gamma_4^{\text{TM}}$  to  $\Gamma_2^{\text{TM}}$  for the transition metal sublattice, and in the  $\text{Tm}$ -based sample, a long-range magnetic order of the  $\text{Tm}^{3+}$  sublattice was found ( $\Gamma_8^R$ ). These results are in excellent agreement with the magnetic susceptibility measurements. No spin reorientation is observed in the  $\text{Lu}$ -based sample for which a magnetization reversal at a compensation temperature  $T_{\text{comp}} = 225$  K was detected. A clear magnetostrictive effect was observed in the samples with  $R = \text{Yb}$  and  $\text{Tm}$  associated with a negative thermal expansion and was assigned to a magnetoelastic effect produced by repulsion between the magnetic moments of neighboring transition metal ions.

DOI: [10.1103/PhysRevB.94.134402](https://doi.org/10.1103/PhysRevB.94.134402)

## I. INTRODUCTION

Rare earth orthoferrites and orthochromites of an  $RM\text{O}_3$  composition, where  $R$  is a lanthanide and  $M$  is  $\text{Fe}$  or  $\text{Cr}$ , have been under exhaustive study for several decades. This is because materials with transition metals and rare earth ions (with unpaired  $d$  and  $f$  electrons, respectively) show a variety of striking effects resulting from the coupling between the two magnetic sublattices.

In these materials, the transition metal sublattice usually orders magnetically at  $T_{N1}$  between 620 and 740 K for orthoferrites and between 120 and 250 K for orthochromites (these temperatures depending on the rare earth ion) into a slightly canted antiferromagnetic structure with a very small ferromagnetic component [1,2]. Generally, the magnetic order for the rare earth sublattices ( $T_{N2}$ ) happens below 10 K, and above this temperature these cations are paramagnetic. However, the rare earth ions undergo the molecular field of the transition metal sublattices, which partially magnetizes them [3]. Consequently, the overall magnetic state at temperatures lower than  $T_{N1}$  has two contributions that interact strongly each other: the small ferromagnetic component of the transition metal sublattices, also called weak ferromagnetism, and the paramagnetic moment of the rare earth ions. The strong interaction between these two contributions of the total magnetic moment could produce two phenomena vastly studied in orthoferrites and orthochromites: magnetization reversal (MR) and spin reorientation (SR).

The MR (also called negative magnetization) is a phenomenon in which the spontaneous magnetization changes its sign at a compensation temperature ( $T_{\text{comp}}$ ) under low applied magnetic field. When the  $R$  ion is magnetic, its sublattice magnetization can orientate parallel or antiparallel to the weak ferromagnetism of the transition metal sublattices. When they are oriented antiparallel, a compensation point is reached at  $T_{\text{comp}}$ , where the moments of the rare earth ions and the transition metal sublattices cancel each other out (e.g., in  $\text{YbCrO}_3$ ,  $\text{GdCrO}_3$ ,  $\text{ErFeO}_3$ , and  $\text{TmFeO}_3$ , among others) [3–5]. A single compound combining MR and magnetoelectric effects could have technological potential for device applications, for example, thermally assisted magnetic random access memories, thermomagnetic switches, and other multifunctional devices [6]. Unfortunately, the low temperature of operation is the main impediment for their potential applications. Therefore, it is necessary to explore materials exhibiting MR at higher temperatures. Some years ago, the presence of MR with highest  $T_{\text{comp}}$  was discovered in perovskites with two magnetic transition metal ions randomly positioned at the  $B$  site and nonmagnetic  $R$  cation at the  $A$  site. Some examples are  $\text{BiFe}_{0.5}\text{Mn}_{0.5}\text{O}_3$  ( $T_{\text{comp}} = 208$  K),  $\text{LaFe}_{0.5}\text{Cr}_{0.5}\text{O}_3$  ( $T_{\text{comp}} = 210$  K), and  $\text{YFe}_{0.5}\text{Cr}_{0.5}\text{O}_3$  ( $T_{\text{comp}} = 260$  K) [6–8]. The unusual behavior of these compounds is explained on a simple model comprising the isotropic superexchange and the antisymmetric Dzyaloshinskii-Moriya (DM) interactions [9,10].

Furthermore, the transition metal sublattice contributions being much less anisotropic than the rare earth contributions, their interaction leads to a whole series of SR transitions, in which the transition metal spin system rotates with respect to the crystal axis [3,11]. These transitions were widely

\*Corresponding author: carbonio@fcq.unc.edu.ar

studied in orthoferrites and orthochromites [2,12–14]. Also, this phenomenon was observed in the perovskite family  $\text{YFe}_{1-x}\text{Mn}_x\text{O}_3$  ( $0 \leq x \leq 0.45$ ) with the two magnetic transition metal ions  $\text{Fe}^{3+}$  and  $\text{Mn}^{3+}$  randomly positioned at the *B* site, and the nonmagnetic cation  $\text{Y}^{3+}$  at the *A* site [15]. Recently it was found that this phenomenon also plays an important role in multiferroic and magnetoelectric materials [13,16–19].

For these reasons we decided to synthesize and study the magnetic behavior and magnetic structure for the series of compounds  $R\text{Fe}_{0.5}\text{Cr}_{0.5}\text{O}_3$  ( $R = \text{Lu}, \text{Yb}, \text{ and Tm}$ ). We refine their crystal and magnetic structures using neutron powder diffraction (NPD) and measure magnetization vs  $T$  (from 4 to 400 K) and vs  $H$  up to 5 T (or 9 T). For these mixed Fe/Cr perovskites, when the *A* site is occupied by a paramagnetic rare earth cation, spin reorientation phenomena have been observed, which are linked with negative thermal expansions. Furthermore, even for diamagnetic *A*-site rare earth ions, a compensation point is evidenced, confirming that the *B*-site mixed occupancy by Fe/Cr ions is sufficient to generate magnetization reversal. Interestingly, a negative thermal expansion phenomenon for the Yb- and Tm-based samples below the spin reorientation transition is observed from the neutron diffraction analysis. Negative thermal expansion (NTE) is a phenomenon where a lattice expands upon cooling. This is rather anomalous and occurs in very few compounds, and the understanding of its anisotropy is still poor [20]. We tentatively assigned the NTE to a magnetoelastic effect produced by repulsion between the magnetic moments of neighboring transition metal ions.

## II. EXPERIMENTAL PROCEDURE

$R\text{Fe}_{0.5}\text{Cr}_{0.5}\text{O}_3$  ( $R = \text{Lu}, \text{Yb}, \text{ and Tm}$ ) samples were prepared in polycrystalline form by a wet chemical method. A very reactive precursor was prepared starting from an aqueous solution of the metal ions and citric acid. Stoichiometric amounts of analytical grade  $\text{R}_2\text{O}_3$ ,  $\text{Fe}(\text{NO}_3)_3 \cdot 9\text{H}_2\text{O}$  and  $\text{Cr}(\text{NO}_3)_3 \cdot 9\text{H}_2\text{O}$  were dissolved in citric acid with some drops of concentrated  $\text{HNO}_3$  to facilitate the dissolution of the rare earth oxides. The citrate solution was slowly evaporated, leading to an organic resin that contained a homogeneous distribution of the involved cations. This resin was dried at 120 °C and then decomposed at 600 °C for 12 h in air, with the aim of eliminating the organic matter. This treatment produced homogeneous and very reactive precursor materials that were finally treated at 1050 °C in air for 12 h.

The x-ray powder diffraction (XRPD) patterns were recorded at room temperature with a PANalytical X'Pert PRO diffractometer (in Bragg-Brentano geometry with  $\text{Cu-K}\alpha$  radiation). For the structure refinements, the XRPD data were collected in the angular  $2\theta$  range of 5–120° in steps of 0.02° and with a collecting time of 10 s/step. NPD experiments were carried out with the powder diffractometer D20 [ $\lambda = 1.35915(2)$  Å] at the Institute Laue-Langevin (ILL) in Grenoble (France). To study the crystallographic and magnetic structures, high-resolution NPD patterns were collected at 300 and 4 K with [8.0° to 160°]  $2\theta$  range and 0.1° increments. The data collection time was approximately 3 h. For the analysis

of thermal evolution, a set of NPD patterns was collected in the temperature range 4.2 to 300 K.

The refinements of crystal structures (from XRPD and NPD data) and magnetic structures (using NPD data) were performed by using the Rietveld method [21] with the FULLPROF program [22]. A Thompson-Cox-Hastings pseudo-Voigt function was chosen to generate the shape of the diffraction peaks. The following parameters were refined: scale factor, background coefficients, zero shift, peak shape parameters, unit cell parameters, atomic positions, isotropic thermal factors, and occupancies of the rare earth and transition metal cations.

The magnetic measurements were performed using a commercial MPMS-5S superconducting quantum interference device magnetometer on powdered samples in capsules, warming from 5 to 400 K at 100 Oe in zero-field-cooled and field-cooled (ZFC-FC) modes, and isothermal loops were performed from 0 to +5 T and then down to –5 T and, to finish, back to 0.

## III. RESULTS

### A. Crystallographic characterizations

$R\text{Fe}_{0.5}\text{Cr}_{0.5}\text{O}_3$  ( $R = \text{Lu}, \text{Yb}, \text{ and Tm}$ ) compounds were obtained as pure orange/brown, well-crystallized powders.

The NPD data of  $R\text{Fe}_{0.5}\text{Cr}_{0.5}\text{O}_3$  at 300 K were correctly refined using the  $Pbnm$  (No. 62) space group ( $Z = 4$ ) with  $a_p\sqrt{2}, a_p\sqrt{2}, 2a_p$  cell parameters ( $a_p$  referring to the ideal cubic perovskite). In this structure  $R^{3+}$  cations and  $\text{O}^{2-}$  (1) anions occupy the  $4c$  ( $x, y, 1/4$ ) sites, and  $\text{Fe}^{3+}/\text{Cr}^{3+}$  cations are randomly distributed at the  $4b$  ( $0, 1/2, 0$ ) sites, and  $\text{O}^{2-}$  (2) anions occupy the general positions  $8d$  ( $x, y, z$ ). To obtain the chemical formula of these  $R\text{Fe}_{0.5}\text{Cr}_{0.5}\text{O}_3$  compounds, the Fe/Cr occupancy in the  $4b$  site was refined since this could not be performed based on XRPD data because the x-ray

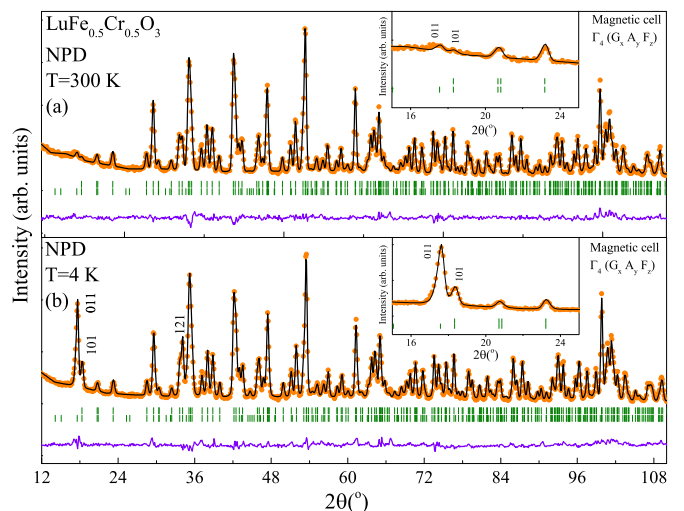


FIG. 1. Observed (orange circles) and calculated (solid black line) NPD patterns at (a) 300 K and (b) 4 K with  $\lambda = 1.35915(2)$  Å for the  $\text{LuFe}_{0.5}\text{Cr}_{0.5}\text{O}_3$  sample. The two series of tick marks correspond to the nuclear Bragg reflections and the magnetic peaks. The difference pattern is plotted at the bottom (violet solid line). Insets: Zoom view of the low-angle region.

TABLE I. Unit cell parameters, atomic positions, occupancies, displacement factors, reliability factors, and refined composition obtained from NPD at 4 K and 300 K for  $R\text{Fe}_{0.5}\text{Cr}_{0.5}\text{O}_3$ .

| <i>R</i>   | Lu   |                              | Yb   |                              | Tm   |                              |
|--|--|------------------------------|--|------------------------------|--|------------------------------|
|  | 300 K  | 4 K                          | 300 K  | 4 K                          | 300 K  | 4 K                          |
| <i>a</i> (Å)                                     | 5.1967(4)  | 5.1861(3)                    | 5.2169(3)  | 5.2081(2)                    | 5.2331(3)  | 5.2297(5)                    |
| <i>b</i> (Å)                                     | 5.5270(5)  | 5.5228(4)                    | 5.5375(2)  | 5.5332(4)                    | 5.5442(4)  | 5.5327(2)                    |
| <i>c</i> (Å)                                     | 7.5195(3)  | 7.5064(2)                    | 7.5320(5)  | 7.5122(5)                    | 7.5468(2)  | 7.5343(4)                    |
| <i>V</i> (Å <sup>3</sup> )                       | 215.976(4)   | 214.994(5)                   | 217.593(6)   | 216.487(3)                   | 218.964(4)   | 218.007(3)                   |
| <i>R</i> 4 <i>c</i> ( <i>x</i> , <i>y</i> , 1/4) |  |                              |  |                              |  |                              |
| <i>x</i>   | 0.5188(4)  | 0.5189(5)                    | 0.5182(4)  | 0.5202(4)                    | 0.5181(5)  | 0.5197(5)                    |
| <i>y</i>   | 0.5703(3)  | 0.5715(4)                    | 0.5697(2)  | 0.5706(3)                    | 0.5684(3)  | 0.5689(3)                    |
| <i>B</i> (Å <sup>2</sup> )                       | 0.66(4)  | 0.68(5)                      | 0.74(4)  | 0.40(5)                      | 0.72(3)  | 0.52(4)                      |
| (Fe, Cr) 4 <i>b</i> (0, 1/2, 0)                  |  |                              |  |                              |  |                              |
| <i>B</i> (Å <sup>2</sup> )                       | 0.641(3)   | 0.589(4)                     | 0.639(3)   | 0.499(5)                     | 0.601(3)   | 0.604(4)                     |
| Occupancy (%)                                    | 0.47(2)/0.53(2)  | 0.47(2)/0.53(2) <sup>a</sup> | 0.50(3)/0.50(2)  | 0.50(3)/0.50(2) <sup>a</sup> | 0.47(2)/0.53(3)  | 0.47(2)/0.53(3) <sup>a</sup> |
| O1 4 <i>c</i> ( <i>x</i> , <i>y</i> , 1/4)       |  |                              |  |                              |  |                              |
| <i>x</i>   | 0.3830(4)  | 0.3808(3)                    | 0.3858(4)  | 0.3853(5)                    | 0.3871(4)  | 0.3845(2)                    |
| <i>y</i>   | −0.0434(4)   | −0.0424(4)                   | −0.0434(4)   | −0.0430(3)                   | −0.0405(4)   | −0.0395(4)                   |
| <i>B</i> (Å <sup>2</sup> )                       | 0.66(4)  | 0.39(5)                      | 0.61(3)  | 0.30(2)                      | 0.64(3)  | 0.38(3)                      |
| O2 8 <i>d</i> ( <i>x</i> , <i>y</i> , <i>z</i> ) |  |                              |  |                              |  |                              |
| <i>x</i>   | 0.6896(3)  | 0.6897(4)                    | 0.6896(3)  | 0.6891(3)                    | 0.6912(3)  | 0.6923(3)                    |
| <i>y</i>   | 0.3062(4)  | 0.3046(3)                    | 0.3065(3)  | 0.3055(4)                    | 0.3047(4)  | 0.3025(5)                    |
| <i>z</i>   | 0.0592(2)  | 0.0603(4)                    | 0.0585(2)  | 0.0593(5)                    | 0.0573(3)  | 0.0591(4)                    |
| <i>B</i> (Å <sup>2</sup> )                       | 0.78(3)  | 0.66(5)                      | 0.78(3)  | 0.50(3)                      | 0.78(3)  | 0.67(4)                      |
| Reliability factors                              |  |                              |  |                              |  |                              |
| $\chi^2$   | 4.32   | 8.67                         | 14.8   | 11.3                         | 9.88   | 9.39                         |
| $R_p$ (%)  | 11.2   | 11.1                         | 8.63   | 7.39                         | 10.8   | 10.2                         |
| $R_{wp}$ (%)                                     | 9.98   | 10.1                         | 8.99   | 7.42                         | 9.70   | 9.64                         |
| $R_{exp}$ (%)                                    | 4.80   | 3.42                         | 2.34   | 2.21                         | 3.08   | 3.15                         |
| $R_{Bragg}$ (%)                                  | 5.70   | 7.85                         | 6.28   | 4.50                         | 7.48   | 7.07                         |
| $R_{Mag}$ (%)                                    | 12.7   | 7.02                         | 4.59   | 8.01                         | 11.5   | 8.21                         |
| Refined composition                              | LuFe <sub>0.47</sub> Cr <sub>0.53</sub> O <sub>3</sub> |                              | YbFe <sub>0.50</sub> Cr <sub>0.50</sub> O <sub>3</sub> |                              | TmFe <sub>0.47</sub> Cr <sub>0.53</sub> O <sub>3</sub> |                              |

<sup>a</sup>The occupancies were fixed at the 300 K values.

scattering factors for Fe<sup>3+</sup> and Cr<sup>3+</sup> ions are very similar. However, these occupancies can be perfectly determined in a very precise way by using NPD because of the high difference in the scattering lengths of Fe and Cr (0.945 and 0.364 fm, respectively). The good agreement between the observed and calculated patterns of LuFe<sub>0.5</sub>Cr<sub>0.5</sub>O<sub>3</sub> at 300 K is illustrated in Fig. 1(a). Table I summarizes the unit cell, atomic positions, occupancies, atomic displacement parameters, and reliability factors obtained from NPD data of the  $R\text{Fe}_{0.5}\text{Cr}_{0.5}\text{O}_3$  at 300 and 4 K. Additionally, Table I shows the calculated chemical formulas obtained for the samples, which are in an excellent agreement with the nominal compositions. As can be seen in Table I, the lattice parameters of the Lu- and Yb-based samples are consistent with the previously reported values [23].

As shown in Fig. 1(a), some reflections in the room temperature NPD pattern are not indexed with the  $Pbnm$  space group. For instance the (011) reflection forbidden in  $Pbnm$

is observed even at 300 K with a very small intensity [see inset of Fig. 1(a)]. These peaks are magnetic reflections, and the magnetic structure refinements will be discussed in the following sections.

## B. Magnetic measurements

ZFC and FC dc magnetic susceptibility curves as a function of temperature were measured in warming for all the members [Figs. 2(a), 2(b), and 2(c)] of the family under an applied magnetic field of 100 Oe. The magnetic behavior of the  $R\text{Fe}_{0.5}\text{Cr}_{0.5}\text{O}_3$  compounds is highly dependent on the  $R^{3+}$  cation and decreasing temperature; all compounds show an increase in susceptibility just below room temperature, suggesting the onset of magnetic ordering ( $T_{N1}$ ). However, the FC and ZFC curves tend to merge far above this ordering temperature, as can be seen in the inset of Fig. 2(b) for the Yb-based sample (shown as an example), suggesting the

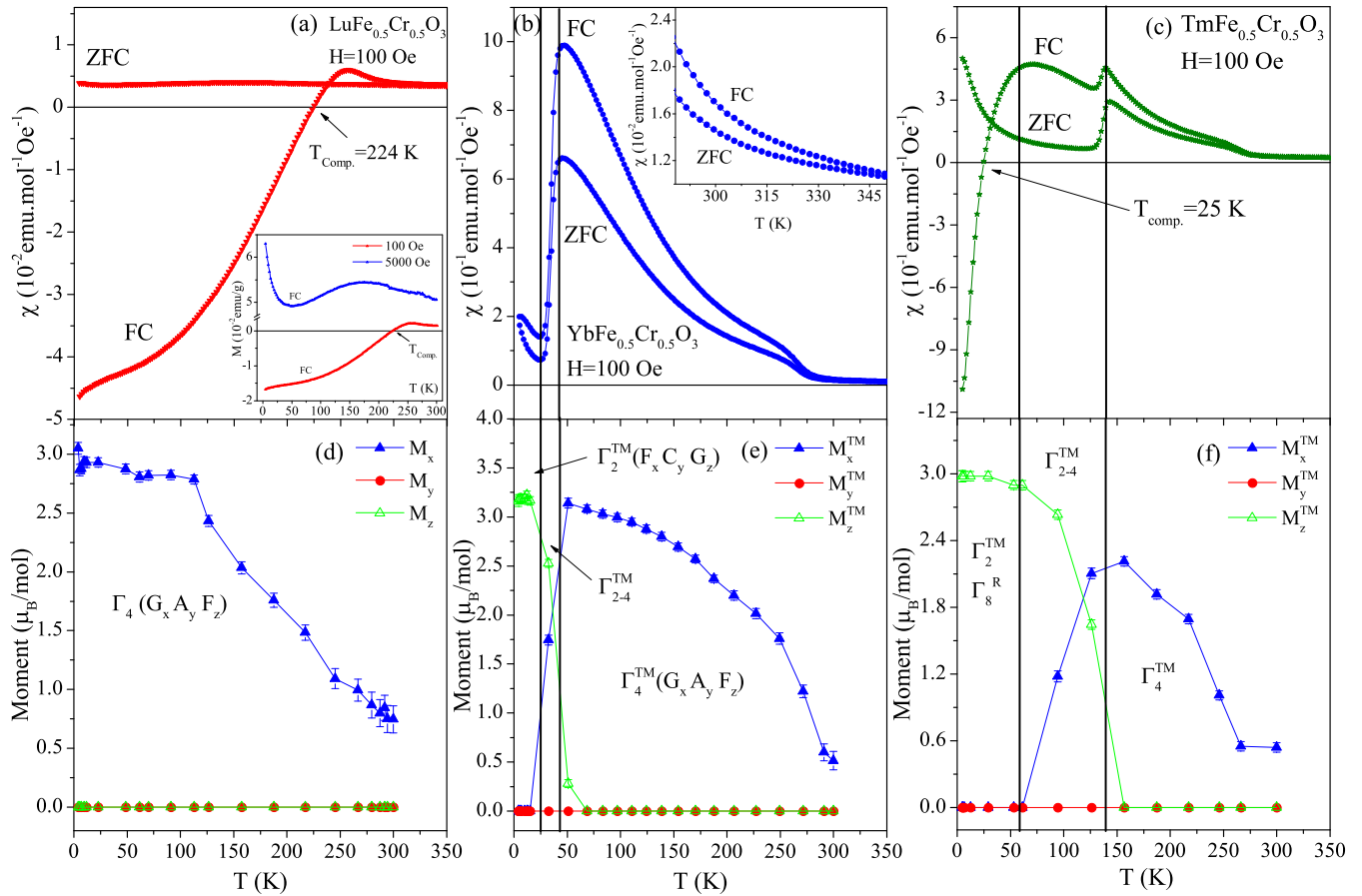


FIG. 2. Upper panel: thermal evolution of the ZFC and FC magnetic susceptibilities for  $R\text{Fe}_{0.5}\text{Cr}_{0.5}\text{O}_3$  compounds measured under an applied magnetic field of 100 Oe, where  $R$  is (a) Lu, (b) Yb, and (c) Tm. Lower panel: thermal evolution of the magnetic moment components obtained from NPD for  $R\text{Fe}_{0.5}\text{Cr}_{0.5}\text{O}_3$  compounds, where  $R$  is (d) Lu, (e) Yb, and (f) Tm. Inset of panel (a): Comparison between the thermal evolution of the FC magnetization measured at 100 Oe and 5000 Oe for  $\text{LuFe}_{0.5}\text{Cr}_{0.5}\text{O}_3$ . Inset of panel (b): Zoom view of the high-temperature range for the ZFC-FC curve of the Yb-based sample.

presence of already existing magnetically ordered regions. This will be discussed in connection to the magnetic structure (see the following section). Also, below  $T_{N1}$ , ZFC and FC curves diverge on decreasing temperature.

In the case of  $\text{LuFe}_{0.5}\text{Cr}_{0.5}\text{O}_3$  (the only nonmagnetic rare earth among those studied), the magnetic order started at  $T_{N1} \sim 290$  K, and the FC magnetic susceptibility reached a maximum at 260 K. Then, the FC magnetic susceptibility drops and crosses the zero value of magnetization at  $T_{\text{comp}} = 224$  K, reaching negative values (MR phenomenon). As expected, the magnetic behavior of  $\text{LuFe}_{0.5}\text{Cr}_{0.5}\text{O}_3$  is very similar to the behavior reported for  $\text{YFe}_{0.5}\text{Cr}_{0.5}\text{O}_3$  [6], since the magnetism only comes from the  $\text{Fe}^{3+}/\text{Cr}^{3+}$  magnetic sublattice. The compensation temperature observed in  $\text{LuFe}_{0.5}\text{Cr}_{0.5}\text{O}_3$  in the measurement at 100 Oe is suppressed at higher  $H$  values, as can be observed in the inset of Fig. 2(a). This suggests that at low  $H$  values the net magnetic moments initially aligned in the direction of the applied magnetic field are realigned in the opposite direction of the applied magnetic field when the temperature lowers; instead, when the applied magnetic field is higher, this realignment cannot be performed because the applied magnetic field is strong enough to keep the alignment parallel to it. In a paper by Dasari *et al.* [9], the

competing character of DM interactions is used in a mean field approximation to explain the field cooling curves of polycrystalline  $\text{YFe}_{1-x}\text{Cr}_x\text{O}_3$ . Besides, in a recent paper [10], we performed Monte Carlo simulations in a classical model for  $R\text{Fe}_{1-x}\text{Cr}_x\text{O}_3$  with  $R = \text{Y}$  and Lu, comparing the numerical simulations with experiments and mean field calculations. In both cases, the dependence of magnetization as a function of temperature for the entire range of compositions is explained by the interplay of DM interactions of Fe-O-Fe, Cr-O-Cr, and Cr-O-Fe; for intermediate compositions, MR is predicted for low  $H$  values in FC modes only.

In the other samples ( $R = \text{Yb}$  and Tm), the magnetic order starts at  $T_{N1} \sim 280$  K, but what happens below this temperature is very different compared with the Lu sample [see Figs. 2(b) and 2(c)]. In the case of  $\text{YbFe}_{0.5}\text{Cr}_{0.5}\text{O}_3$ , below  $T_{N1}$  the ZFC and FC magnetic susceptibility curves separate and both increase, reaching a maximum at approximately 50 K; then, magnetic susceptibility drops, but the magnetization never reaches negative values. Finally, the magnetic susceptibility in both curves increases slightly again in the temperature range from 25 to 5 K. In the case of the sample with Tm [Fig. 2(c)], the behavior of the magnetic susceptibility below 280 K is similar to the behavior observed in the  $\text{YbFe}_{0.5}\text{Cr}_{0.5}\text{O}_3$

sample down to 140 K, but then it exhibits some important differences. First, the ZFC and FC magnetic susceptibility curves in  $\text{TmFe}_{0.5}\text{Cr}_{0.5}\text{O}_3$  have a peak at approximately 140 K, and second, in this sample, the FC magnetic susceptibility curve reaches negative values below  $T_{\text{comp}} = 25$  K. In this case, as Tm is a magnetic ion and the rare earth sublattice magnetization is oriented antiparallel to the transition metal sublattice weak ferromagnetic (WF) components, a compensation point is observed at lower temperatures than observed in the Lu sample. The difference between Yb and Tm, with the latter having negative values for the FC curve, will be discussed later.

Isothermal magnetization curves were measured at 5 K. The curves are displayed in Fig. 3 for the three samples. The magnetization curve for the sample with the nonmagnetic rare earth  $\text{Lu}^{3+}$  (note that this curve was multiplied by a factor of 50) presents linear dependence with  $H$  and the values of magnetization are two orders of magnitude lower than the other studied samples ( $R = \text{Yb}$  and  $\text{Tm}$ ). On the contrary, a nonlinear  $M$  vs  $H$  behavior is observed for the Yb- and Tm-based samples. This linear behavior in  $R = \text{Lu}$  can be associated with the antiferromagnetic (AFM) ordering with complete compensation of the magnetic moments of  $\text{Fe}^{3+}$  and  $\text{Cr}^{3+}$  ions. The nonlinear response of the Yb- and Tm-based samples is understood as a complex behavior that includes the AFM (or WF) order of the Fe/Cr sublattice and, superimposed to this signal, the paramagnetic response of the rare earth, which is not linear for paramagnetic  $\text{Tm}^{3+}$  ions.

### C. Determination of the magnetic structure

As stated in the ‘‘Magnetic measurements’’ section, the onset of a magnetic ordering ( $T_{N1}$ ) takes place at temperatures close to room temperature for the three  $R\text{Fe}_{0.5}\text{Cr}_{0.5}\text{O}_3$  samples. However, the NPD patterns collected at 300 K showing magnetic reflections [Fig. 1(a)] indicate that short-range ordered regions exist above  $T_{N1}$ , in agreement with the ZFC-FC curves, merging well above  $T_{N1}$  [see inset of Fig. 2(b)]. As the

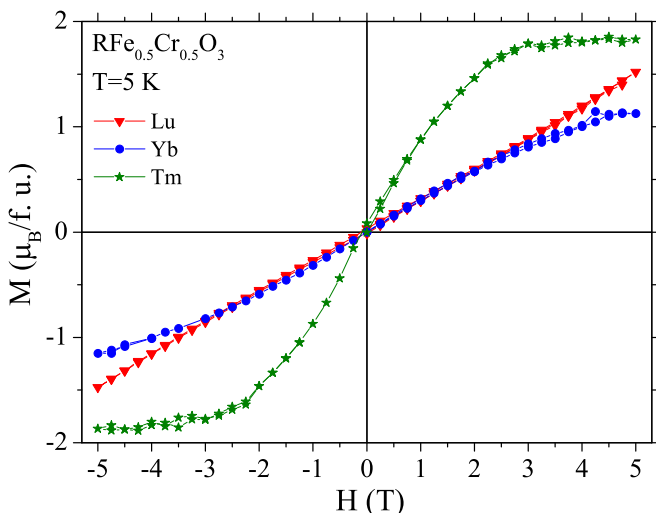


FIG. 3. Isothermal magnetization curves for  $R\text{Fe}_{0.5}\text{Cr}_{0.5}\text{O}_3$  samples measured at  $T = 5$  K. Note that the  $M$  vs  $H$  curve for  $\text{LuFe}_{0.5}\text{Cr}_{0.5}\text{O}_3$  was multiplied by a factor of 50.

B cations are disordered in these perovskites, this can be understood by the presence of small regions whose magnetism is dominated by  $\text{Fe}^{3+}\text{-O-Fe}^{3+}$  superexchange.

Initially, the magnetic structures were determined from the 4 K data. For all the samples, the (101) and (121) reflections allowed in  $Pbnm$  are more intense at lower temperatures, and the intensity of (011) reflection forbidden in  $Pbnm$  strongly increases (as shown in Fig. 4). The different magnetic groups associated with the propagation vector  $k = (0,0,0)$  and compatible with the  $Pbnm$  space group were tabulated by Bertaut [24] and led for the transition elements ( $B$  site of the perovskite) to four irreducible representations allowing a nonzero magnetic contribution. The  $B$ -site magnetic cations are present at  $4b$  sites at positions  $S1(1/2,0,0)$ ,  $S2(0,1/2,0)$ ,  $S3(1/2,0,1/2)$  and  $S4(0,1/2,1/2)$ . Four base vectors representing the possible magnetic modes of coupling can be expressed according to Bertaut’s notation,

$$F = +S1 + S2 + S3 + S4,$$

$$G = +S1 - S2 - S3 + S4,$$

$$C = +S1 - S2 + S3 - S4,$$

$$A = +S1 + S2 - S3 - S4,$$

The four irreducible representations known for orthoferrites can be represented in terms of vector components  $F$ ,  $G$ ,  $C$ , and  $A$  along three crystallographic directions. According to Bertaut’s notations, these are defined as  $\Gamma_1(A_x G_y C_z)$ ,  $\Gamma_2(F_x C_y G_z)$ ,  $\Gamma_3(C_x F_y A_z)$ , and  $\Gamma_4(G_x A_y F_z)$ . On the other hand, the  $A$ -site (rare earth site) magnetic cations are present at  $4c$  sites at positions  $S1(x, y, 1/4)$ ,  $S2(x, y, 3/4)$ ,  $S3(x, y, 3/4)$ , and  $S4(x, y, 1/4)$ , and the irreducible representations are defined as  $\Gamma_1(00C_z)$ ,  $\Gamma_2(F_x C_y 0)$ ,  $\Gamma_3(C_x F_y 0)$ ,  $\Gamma_4(00F_z)$ ,  $\Gamma_5(G_x A_y 0)$ ,  $\Gamma_6(00A_z)$ ,  $\Gamma_7(00G_z)$ , and  $\Gamma_8(A_x G_y 0)$ .

For the  $\text{LuFe}_{0.5}\text{Cr}_{0.5}\text{O}_3$  sample, the neutron patterns were modeled with the irreducible representation  $\Gamma_4(G_x A_y F_z)$

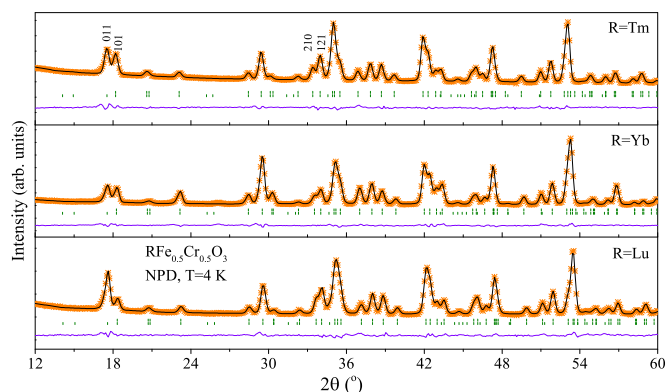


FIG. 4. Observed (orange crosses) and calculated (solid black line) NPD patterns at 4 K with  $\lambda = 1.35915(2)$  Å for  $R\text{Fe}_{0.5}\text{Cr}_{0.5}\text{O}_3$  ( $R = \text{Lu}, \text{Yb}$ , and  $\text{Tm}$ ) samples. The two series of tick marks in each pattern correspond to the nuclear Bragg reflections and the magnetic peaks. The difference pattern is plotted at the bottom (violet solid line).

TABLE II. Magnetic moment components  $M_x$ ,  $M_y$ , and  $M_z$  and magnetic moment module obtained from NPD at 4 and 300 K for  $R\text{Fe}_{0.5}\text{Cr}_{0.5}\text{O}_3$  samples.

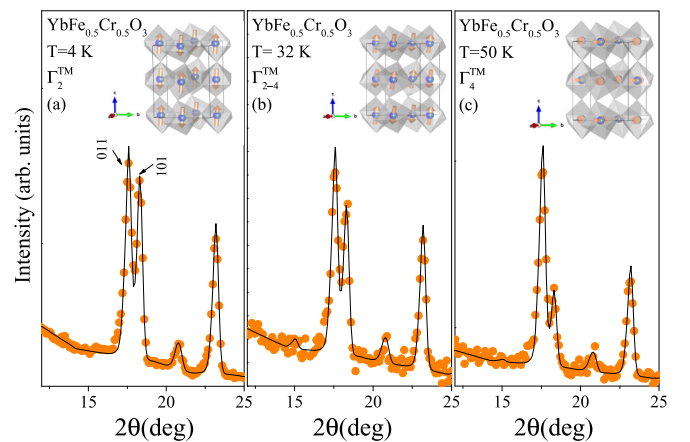
| Irreducible representation                 |       | Lu                      |                         | Yb                      |                         | Tm                      |                         |
|--|-------|-------------------------|-------------------------|-------------------------|-------------------------|-------------------------|-------------------------|
|  |       | 300 K                   | 4 K                     | 300 K                   | 4 K                     | 300 K                   | 4 K                     |
|  |       | $\Gamma_4(G_x A_y F_z)$ | $\Gamma_4(G_x A_y F_z)$ | $\Gamma_4(G_x A_y F_z)$ | $\Gamma_2(F_x C_y G_z)$ | $\Gamma_4(G_x A_y F_z)$ | $\Gamma_2(F_x C_y G_z)$ |
| $\text{Fe}^{3+}/\text{Cr}^{3+}$ sublattice | $M_x$ | 0.75(5)                 | 3.05(2)                 | 0.5(1)                  | 0                       | 0.54(8)                 | 0                       |
|  | $M_y$ | 0                       | 0                       | 0                       | 0                       | 0                       | 0                       |
|  | $M_z$ | 0                       | 0                       | 0                       | 3.13(2)                 | 0                       | 2.98(4)                 |
|  | $ M $ | 0.75                    | 3.05                    | 0.5                     | 3.13                    | 0.54                    | 2.98                    |
| Irreducible representation                 |       | —                       | —                       | —                       | —                       | —                       | $\Gamma_8(A_x G_y 0)$   |
| $R^{3+}$ sublattice                        | $M_x$ | —                       | —                       | —                       | —                       | —                       | 0.9(1)                  |
|  | $M_y$ | —                       | —                       | —                       | —                       | —                       | 0                       |
|  | $M_z$ | —                       | —                       | —                       | —                       | —                       | 0                       |
|  | $ M $ | —                       | —                       | —                       | —                       | —                       | 0.9                     |

along all [4–300 K] temperature range. In this sample, the only magnetic ions are  $\text{Fe}^{3+}$  and  $\text{Cr}^{3+}$  and are randomly distributed at the  $4b$  site. Figures 1(a) and 1(b) show the good agreement between the observed and calculated NPD patterns at 300 and 4 K, respectively. The thermal evolution of the magnetic moment components ( $M_x$ ,  $M_y$ , and  $M_z$ ) at the transition metal are displayed in Fig. 2(d), and Table II reports the values obtained at 4 and 300 K. As stated earlier, the neutron patterns were modeled with the irreducible representation  $\Gamma_4(G_x A_y F_z)$  across all analyzed temperature range. Actually, using  $\Gamma_4(G_x A_y F_z)$  across all temperature ranges shows that the moments are mainly oriented along the  $x$  direction [Fig. 2(d)] with a G-type AFM arrangement (i.e., the next neighbors are AFM coupled in the three directions). A ferromagnetic component along the  $c$  axis and an AFM type A arrangement along  $b$  axis are allowed by symmetry, but the calculated  $M_y$  and  $M_z$  components are close to zero, with large standard deviation, and thus were supposed null and fixed to zero in the final refinements. Furthermore, in agreement with the magnetic measurements, no spin reorientation is detected from the neutron data analysis.

The low-angle region of the refined NPD patterns for  $\text{YbFe}_{0.5}\text{Cr}_{0.5}\text{O}_3$  at 4, 32, and 50 K are shown in Fig. 5 (the 4, 32, 50, and 300 K complete patterns are given in Fig. SI-1 in the Supplemental Material [25]). The magnetic reflections that increase in intensity when temperature decreases are the same as for the Lu sample. It may be noted in Fig. 5 that the intensity ratio between the (011) and (101) reflections changes with temperature. When temperature decreases from 50 to 4 K, the intensity of the (101) reflection increases gradually, whereas the (011) reflection remains almost constant. This reflects the spin reorientation indicated in the magnetization data [see Fig. 2(b)]. The spin reorientation observed when temperature decreases corresponds to the sequence of transitions  $\Gamma_4(G_x A_y F_z) \rightarrow \Gamma_{2-4}(G_{x,z} A_y - C_y F_{z,x}) \rightarrow \Gamma_2(F_x C_y G_z)$ , which takes the system from  $\Gamma_4(G_x A_y F_z)$  with magnetic moment along the  $x$  axis in the G-type AFM arrangement to another configuration  $\Gamma_2(F_x C_y G_z)$ , keeping a G-type AFM arrangement but along the  $z$  axis. As shown in Figs. 2(b) and 2(e), this transition occurs from  $T_1 = 50$  K to  $T_2 = 25$  K. In this temperature range, the magnetic moments rotate from the  $a$  axis toward the  $c$  axis, staying in the ( $a$ ,  $c$ )

plane (both magnetic structures are shown in Fig. 5). The excellent agreement between the experimental and calculated NPD patterns shown in Fig. 5 (and in Fig. SI-1 [25]) was obtained considering only the long-range magnetic order of the transition metal sublattices, and it was not necessary to include a magnetic structure for the rare earth sublattice, even at 4 K (see Table II). Figure SI-2 in the Supplemental Material [25] presents three calculated NPD patterns, with the measured one at 32 K refined with the three  $\Gamma_2, \Gamma_{2-4}$ , and  $\Gamma_4$  irreducible representations to show that the best fit is obtained with the  $\Gamma_{2-4}$  representation at that temperature. Figures 2(b) and 2(e) illustrate the agreement between macroscopic magnetic measurements and temperature dependence of the magnetic moments: the spin reorientation temperature range determined by NPD is in perfect agreement with the shape of the ZFC-FC susceptibility curves.

Zoom views in the low-angle region for the NPD patterns refined for  $\text{TmFe}_{0.5}\text{Cr}_{0.5}\text{O}_3$  at 4, 126, and 157 K are shown in Fig. 6. In the Supplemental Material Fig. SI-3 [25], the complete NPD patterns are given. The behavior of this sample is similar to that observed for the transition metal sublattice in  $\text{YbFe}_{0.5}\text{Cr}_{0.5}\text{O}_3$ , but an important difference


 FIG. 5. Comparison between the intensity of the main magnetic reflections at 4, 32, and 50 K for the  $\text{YbFe}_{0.5}\text{Cr}_{0.5}\text{O}_3$  sample. A view of the refined magnetic structure in each case is shown.

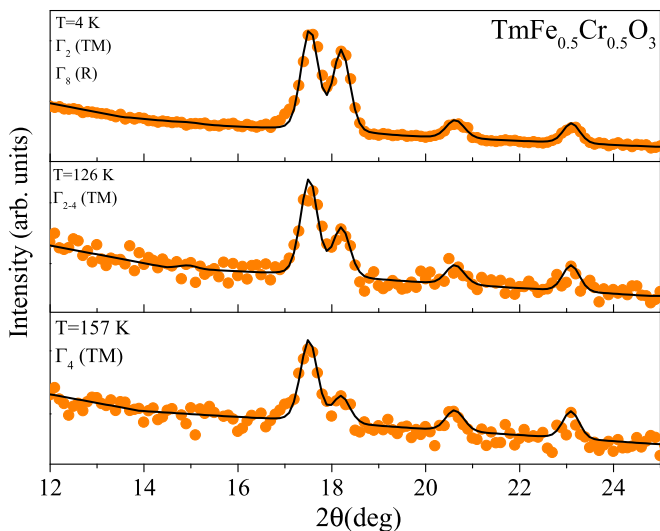


FIG. 6. Comparison between the intensity of the main magnetic reflections at 4, 126, and 157 K for the  $\text{TmFe}_{0.5}\text{Cr}_{0.5}\text{O}_3$  sample.

deals with the rare earth sublattice that also orders magnetically. In  $\text{TmFe}_{0.5}\text{Cr}_{0.5}\text{O}_3$  sample at temperatures below  $\sim 52$  K, a long-range magnetic order of the  $\text{Tm}^{3+}$  sublattice is observed, together with the long-range magnetic order of the transition metals reached at higher temperatures;

therefore, it is necessary to include the  $\text{Tm}^{3+}$  contribution to refine the magnetic structure. As presented in Figs. 2(c) and 2(f), the irreducible representation series that fits the NPD patterns is  $[\Gamma_4(G_x A_y F_z)^{\text{TM}}] \rightarrow [\Gamma_{2-4}(G_{x,z} A_y - C_y F_{z,x})^{\text{TM}}] \rightarrow [\Gamma_2(F_x C_y G_z)^{\text{TM}}/\Gamma_8(A_x G_y 0)^{\text{R}}]$  and these transitions take place from  $T_1 = 140$  to  $T_2 = 52$  K and, as stated above, below 52 K the  $\text{Tm}^{3+}$  sublattice reached a long-range magnetic order. Figure 2(c) and 2(f) show the complementarity between the ZFC-FC curves with the temperature evolution of the magnetic moment obtained by NPD. The spin reorientation temperature range of the transition metals sublattice determined by NPD is consistent with the one determined by magnetization measurements.

#### D. Negative thermal expansion

The temperature dependence of lattice parameters for  $R\text{Fe}_{0.5}\text{Cr}_{0.5}\text{O}_3$  ( $R = \text{Lu}, \text{Yb}$  and  $\text{Tm}$ ) was examined by cooling from 300 to 4 K. The results for  $\text{YbFe}_{0.5}\text{Cr}_{0.5}\text{O}_3$  (between 90 and 4 K) and  $\text{TmFe}_{0.5}\text{Cr}_{0.5}\text{O}_3$  (between 160 and 4 K) are shown in Figs. 7(a) and 7(b), respectively. The curves corresponding to  $\text{LuFe}_{0.5}\text{Cr}_{0.5}\text{O}_3$  are shown in Fig. SI-4 in the Supplemental Material [25]. In  $\text{LuFe}_{0.5}\text{Cr}_{0.5}\text{O}_3$  the expected thermal expansion (TE) of the unit cell volume when temperature increases is observed. In  $\text{YbFe}_{0.5}\text{Cr}_{0.5}\text{O}_3$ , a NTE phenomenon is evidenced in the temperature range from

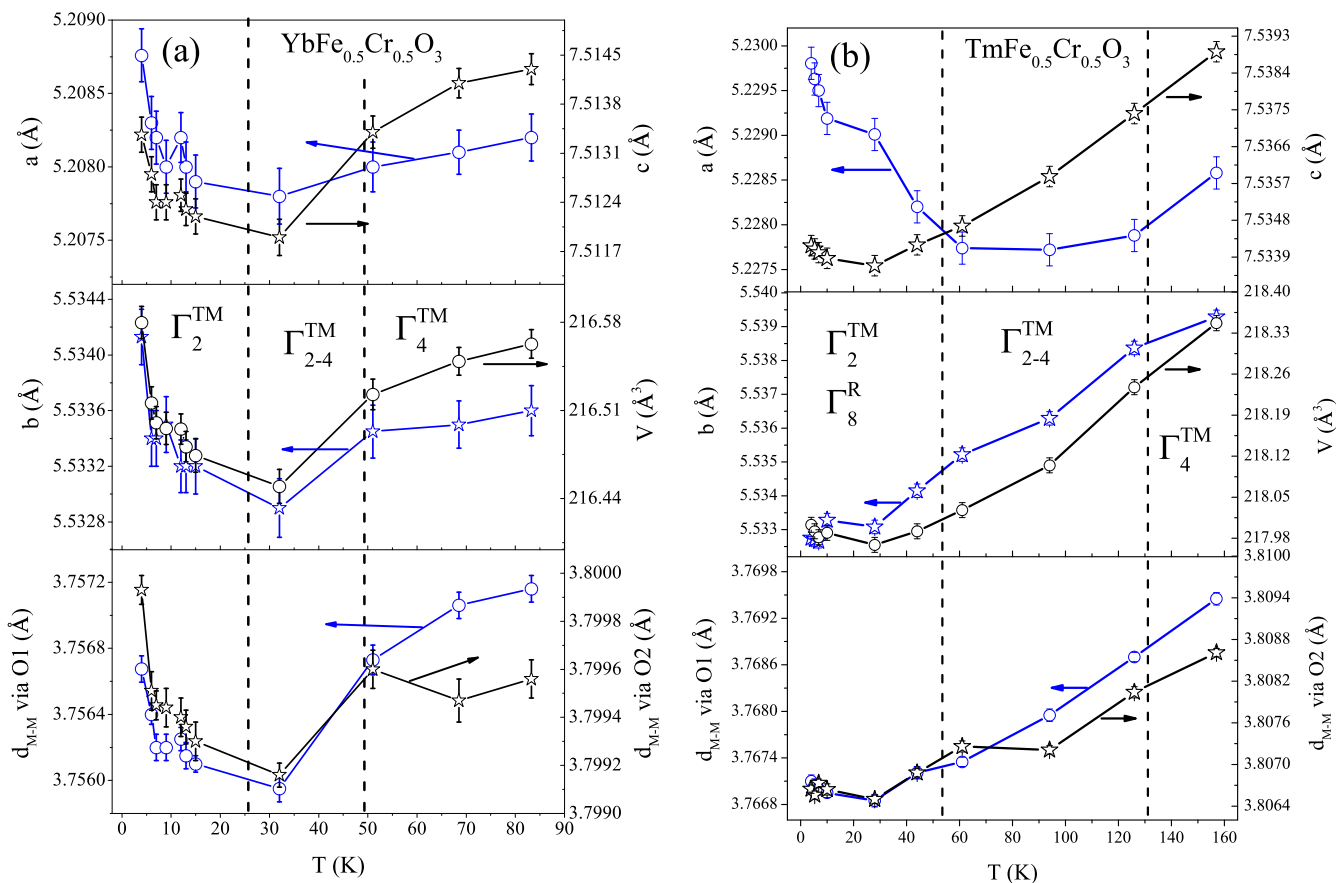


FIG. 7. Temperature dependence of lattice parameters ( $a$ ,  $b$ ,  $c$ , and cell volume) and the metal transition bond length for  $\text{YbFe}_{0.5}\text{Cr}_{0.5}\text{O}_3$  (a) and  $\text{TmFe}_{0.5}\text{Cr}_{0.5}\text{O}_3$  (b).

25 to 4 K, where the magnetic structure of the transition metal ions have a  $\Gamma_2$  irreducible representation, and the magnetic moments are almost along the  $a$  axis. The lattice parameters along the three axes ( $a$ ,  $b$ , and  $c$ ) increase slightly below 25 K by approximately 0.02%, which correspond to approximately a 0.06% volume expansion of the unit cell. The net volume coefficient of the TE ( $\alpha_v$ ) of  $\text{YbFe}_{0.5}\text{Cr}_{0.5}\text{O}_3$  in the temperature range from 25 to 4 K is estimated as  $-2.16 \times 10^{-5}\text{K}^{-1}$ , which gives an average linear coefficient of expansion ( $\alpha_l$ ) of  $-7.20 \times 10^{-6}\text{K}^{-1}$ . The observed volume expansion of  $\text{YbFe}_{0.5}\text{Cr}_{0.5}\text{O}_3$  ( $\sim 0.06\%$ ) is comparable to other oxides for which NTE phenomena are known, as for example  $\text{PrFeAsO}$  [26],  $\text{Co}_3\text{TeO}_6$  [27], or  $\text{Li}_2\text{Ni}(\text{WO}_4)_2$  [28].

In the case of  $\text{TmFe}_{0.5}\text{Cr}_{0.5}\text{O}_3$ , the NTE effect is observed only for the  $a$  (0.04%) and  $c$  axes (0.006%) below  $\sim 52$  K, and it is lower than the observed in  $\text{YbFe}_{0.5}\text{Cr}_{0.5}\text{O}_3$ .

The NTE phenomenon observed in both samples occurs below the spin reorientation transition when the magnetic structure of the transition metals acquired the  $\Gamma_2$  representation. This evidently implies the existence of a strong correlation between these phenomena. Furthermore, the spin reorientation transitions are strongly linked with the interaction between the  $d$  and  $f$  magnetic sublattices, as confirmed by  $\text{Lu}^{3+}$ , for which the reorientation is not observed.

Magnetoelastic volume effects, in which magnetic transitions drive volume changes, have also been widely investigated. For example in  $\text{PrFeAsO}$ , Kimber *et al.* [26] proposed that the NTE originated in the magnetoelastic coupling related to the onset of Fe and Pr magnetic ordering. Another example is  $\text{Li}_2\text{Ni}(\text{WO}_4)_2$ , where a NTE phenomenon is observed below the onset of a commensurate long-range AFM ordering of the Ni magnetic moments, which has been interpreted as a result of competing normal thermal contraction and long-range AFM spin ordering through counterbalanced  $\text{WO}_4$  and  $\text{NiO}_6$  polyhedral local distortion [28].

With the aim to understand the origin of the NTE in our compounds, the temperature dependence of the interatomic distances was analyzed. Figures 7(a) and 7(b) show the temperature dependence of the transition metal  $d_{M-M}$  (via O1 and O2) for  $\text{YbFe}_{0.5}\text{Cr}_{0.5}\text{O}_3$  and  $\text{TmFe}_{0.5}\text{Cr}_{0.5}\text{O}_3$ , respectively. In the case of the Yb sample, a clear elongation of the M-M bonds is observed in the NTE temperature range, but in the Tm sample, a smoother elongation of the M-M distances is observed at very low temperatures. This is in agreement with the much larger NTE for the Yb compound than for the Tm compound. Thus, the NTE could be assigned to a magnetoelastic effect produced by repulsion between the magnetic moments of neighbor transition metal ions.

Analyzing other differences between these two samples, it can be highlighted that in the Tm sample, a long-range magnetic ordering of  $\text{Tm}^{3+}$  is observed below 52 K. In both samples, a spin reorientation happens from  $\Gamma_4(G_x A_y F_z)^{\text{TM}}$  to  $\Gamma_2(F_x C_y G_z)^{\text{TM}}$  representations when temperature decreases.

#### IV. CONCLUSIONS

A systematic study of the crystal and magnetic structure was performed by NPD and magnetization measurements in the family  $R\text{Fe}_{0.5}\text{Cr}_{0.5}\text{O}_3$  ( $R = \text{Lu}, \text{Yb}, \text{and Tm}$ ). The magnetic behavior of the  $R\text{Fe}_{0.5}\text{Cr}_{0.5}\text{O}_3$  is highly dependent on the  $R^{3+}$  cation and the onset of magnetic ordering ( $T_{N1}$ ) takes place at temperatures close to room temperature for the three  $R\text{Fe}_{0.5}\text{Cr}_{0.5}\text{O}_3$  samples. However, the FC and ZFC curves tend to merge far above this ordering temperature, in agreement with the small magnetic reflections observed in the NPD patterns collected at 300 K, indicating that short-range ordered regions whose magnetism is dominated by the  $\text{Fe}^{3+}\text{-O-Fe}^{3+}$  superexchange exist above  $T_{N1}$ .

The NPD study of the magnetic structures shows the occurrence of a progressive spin reorientation from  $\Gamma_4^{\text{TM}}$  to  $\Gamma_2^{\text{TM}}$  for the transition metals in the samples with  $R = \text{Yb}$  and  $\text{Tm}$ ; in the last one, a long-range magnetic ordering of the  $\text{Tm}^{3+}$  is found ( $\Gamma_8^R$ ). These results show excellent agreement with the magnetic susceptibility measurements. When lowering temperature, there is a peak in magnetic susceptibility curves matching the beginning of the spin reorientation; then, when spin reorientation is finished, there is an abrupt fall in the magnetic susceptibility that, in the case of the Tm sample, leads to a magnetization reversal.

$\text{LuFe}_{0.5}\text{Cr}_{0.5}\text{O}_3$  has a completely different behavior. No spin reorientation is observed ( $\Gamma_4^{\text{TM}}$  for all considered temperatures), which is attributed to the fact that  $\text{Lu}^{3+}$  is diamagnetic and has no influence on the transition metal sublattices. Besides, a magnetization reversal with  $T_{\text{comp}} = 225$  K is detected, which comes from the mixed and disordered  $B$ -site occupation by Fe and Cr, implying different  $M\text{-O-M'}$  magnetic interactions.

A clear magnetostrictive effect is observed in the samples with  $R = \text{Yb}$  and  $\text{Tm}$  associated with a negative thermal expansion attributed to a magnetoelastic effect produced by repulsion between the magnetic moments of neighboring transition metal ions.

#### ACKNOWLEDGMENTS

R.E.C. thanks CONICET, PIP No. 11220120100360, the Agencia Nacional de Promoción Científica y Tecnológica (ANPCyT), PICT No. 2013-2149, and the Secretaría de Ciencia y Tecnología de la Universidad Nacional de Córdoba (SECyT-UNC), Project No. 203/14 for support. R.D.S. acknowledges support from ANPCyT, PICT No. 2011-752, CONICET, PIP No. 0490, and SECyT-UNCuyo No. 06/C456. We gratefully acknowledge the ILL (Grenoble, France) for access to the D20 powder diffractometer. F.P. thanks CONICET for a fellowship. R.E.C. and A.M. gratefully acknowledge a collaboration project between CNRS and CONICET (No. PCB I-2014).

[1] L. T. Tsymbal, Ya. B. Bazaliy, V. N. Derkachenko, V. I. Kamenev, G. N. Kakazei, F. J. Palomares, and P. E. Wigen, *J. Appl. Phys.* **101**, 123919 (2007).

[2] Ya. B. Bazaliy, L. T. Tsymbal, G. N. Kakazei, A. I. Izotov, and P. E. Wigen, *Phys. Rev. B* **69**, 104429 (2004).

[3] R. L. White, *J. Appl. Phys.* **40**, 1061 (1969).

- [4] Y. Su, J. Zhang, Z. Feng, L. Li, B. Li, Y. Zhou, Z. Chen, and S. Cao, *J. Appl. Phys.* **108**, 013905 (2010).
- [5] K. Yoshii, *J. Solid State Chem.* **159**, 204 (2001).
- [6] J. Mao, Y. Sui, X. Zhang, Y. Su, X. Wang, Z. Liu, Y. Wang, R. Zhu, Y. Wang, W. Liu, and J. Tang, *Appl. Phys. Lett.* **98**, 192510 (2011).
- [7] P. Mandal, A. Sundaresan, C. N. R. Rao, A. Iyo, P. M. Shirage, Y. Tanaka, Ch. Simon, V. Pralong, O. I. Lebedev, V. Caignaert, and B. Raveau, *Phys. Rev. B* **82**, 100416(R) (2010).
- [8] A. K. Azad, A. Mellergård, S.-G. Eriksson, S. A. Ivanov, S. M. Yunus, F. Lindberg, G. Svensson, and R. Mathieu, *Mater. Res. Bull.* **40**, 1633 (2005).
- [9] N. Dasari, P. Mandal, A. Sundaresan, and N. S. Vidhyadhiraja, *Europhysics Lett.* **99**, 17008 (2012).
- [10] O. V. Billoni, F. Pomiro, S. A. Cannas, C. Martin, A. Maignan, and R. E. Carbonio, *J. Phys.: Condens. Matter* **28**, 476003 (2016).
- [11] T. Yamaguchi, *J. Phys. Chem. Solids* **35**, 479 (1974).
- [12] L. T. Tsymbal, V. I. Kamenev, D. A. Khara, Ya. B. Bazaliy, and P. E. Wigen, *Low Temp. Phys.* **32**, 779 (2006).
- [13] K. R. S. Preethi Meher, A. Wahl, A. Maignan, C. Martin, and O. I. Lebedev, *Phys. Rev. B* **89**, 144401 (2014).
- [14] B. Rajeswaran, D. I. Khomskii, A. K. Zvezdin, C. N. R. Rao, and A. Sundaresan, *Phys. Rev. B* **86**, 214409 (2012).
- [15] P. Mandal, C. R. Serrao, E. Suard, V. Caignaert, B. Raveau, A. Sundaresan, and C. N. R. Rao, *J. Solid State Chem.* **197**, 408 (2013).
- [16] T. Kimura, T. Goto, H. Shintani, K. Ishizaka, T. Arima, and Y. Tokura, *Nature* **426**, 55 (2003).
- [17] N. Hur, S. Park, P. A. Sharma, J. S. Ahn, S. Guha, and S.-W. Cheong, *Nature* **429**, 392 (2004).
- [18] A. K. Zvezdin and A. A. Mukhin, *JETP Lett.* **88**, 505 (2008).
- [19] Y. Tokunaga, N. Furukawa, H. Sakai, Y. Taguchi, T. Arima, and Y. Tokura, *Nat. Mater.* **8**, 558 (2009).
- [20] A. W. Sleight, *Annu. Rev. Mater. Sci.* **28**, 29 (1998).
- [21] H. M. Rietveld, *J. Appl. Crystallogr.* **2**, 65 (1969).
- [22] J. Rodríguez-Carvajal, *Phys. B Condens. Matter* **192**, 55 (1993).
- [23] L. Yuan, K. Huang, C. Hou, W. Feng, S. Wang, C. Zhou, and S. Feng, *New J. Chem.* **38**, 1168 (2014).
- [24] E. F. Bertaut, *Acta Crystallogr. Sect. A* **24**, 217 (1968).
- [25] See Supplemental Material at <http://link.aps.org/supplemental/10.1103/PhysRevB.94.134402> for results of (S1) PND for Yb sample, (S2) zoom view of PND for Yb sample, (S3) PND for Tm sample, and (S4) lattice parameters vs T for Lu sample.
- [26] S. A. J. Kimber, D. N. Argyriou, F. Yokaichiya, K. Habicht, S. Gerischer, T. Hansen, T. Chatterji, R. Klingeler, C. Hess, G. Behr, A. Kondrat, and B. Büchner, *Phys. Rev. B* **78**, 140503 (R) (2008).
- [27] C.-W. Wang, C.-H. Lee, C.-Y. Li, C.-M. Wu, W.-H. Li, C.-C. Chou, H.-D. Yang, J. W. Lynn, Q. Huang, A. B. Harris, and H. Berger, *Phys. Rev. B* **88**, 184427 (2013).
- [28] S. K. Karna, C. W. Wang, R. Sankar, M. Avdeev, A. Singh, I. Panneer Muthuselvam, V. N. Singh, G. Y. Guo, and F. C. Chou, *Phys. Rev. B* **92**, 014413 (2015).